Nat. Hazards Earth Syst. Sci. Discuss., 3, 6271–6319, 2015
www.nat-hazards-earth-syst-sci-discuss.net/3/6271/2015/
doi:10.5194/nhessd-3-6271-2015

Natural Hazards and Earth System Sciences
Open Access
Discussions

Quantification and analysis of geomorphic processes on a recultivated iron ore mine on the Italian island Elba using long-time ground-based LIDAR and photogrammetric data by an UAV

F. Haas[1], L. Hilger[1], F. Neugirg[1], K. Umstädter[1], C. Breitung[1], P. Fischer[2], P. Hilger[1,a], T. Heckmann[1], J. Dusik[1], A. Kaiser[3], J. Schmidt[3], M. Della Seta[4], R. Rosenkranz[4,b], and M. Becht[1]

[1]Chair of Physical Geography, Catholic University of Eichstätt-Ingolstadt, 85072 Eichstätt, Germany
[2]Applied Physical Geography, Catholic University of Eichstätt-Ingolstadt, 85072 Eichstätt, Germany
[3]Soil and Water Conservation Unit, Technical University Bergakademie Freiberg, 09599 Freiberg, Germany
[4]Dipartimento di Scienze della Terra, Universitá degli Studi di Roma “La Sapienza”, 00185 Rome, Italy
[a]now at: Geological survey of Norway NGU, 7040 Trondheim, Norway

[b]now at: University of Bremen, Department of Geosciences, 28359 Bremen, Germany

Received: 21 September 2015 – Accepted: 21 September 2015 – Published: 13 October 2015

Correspondence to: F. Haas (florian.haas@ku.de)

Published by Copernicus Publications on behalf of the European Geosciences Union.

NHESSD
3, 6271–6319, 2015

Abstract

This study aims on the quantification and analysis of geomorphic processes on the barely vegetated slopes of a recultivated iron ore mine on the Italian island Elba using Terrestrial Lasercanning (TLS) and digital photogrammetry by UAV photographs over a period of 5 1/2 years. Beside this the study tried to work out the potential and the limitations of both methods to detect surface changes by geomorphic process dynamic within a natural environment. Both, UAV and TLS show the pattern of the erosion and accumulation processes on the investigated slope quite well, but the calculated amounts differ clearly between the methods. The reasons for these differences could be found in the different accuracies (variable level of detections) of the methods and the different viewing geometries. Both effects have an impact on the detectable process dynamic over different time scales on the slope and their calculated amounts, which in both cases can lead to an underestimation of erosion and accumulation by fluvial processes.

1 Introduction

Fluvial erosion plays a major role for the geomorphic forming on steep slopes (Bryan, 2000) in agricultural (Diodato and Bellocchi, 2000; Auerswald et al., 2000) as well as in natural landscapes. In the Mediterranean regions the special climatic conditions in combination with the topography and the lithological conditions lead to intensive gullying and badland generation (Della Seta et al., 2009; Aucelli et al., 2012), with high intensities on steep and barely vegetated slopes (Haas et al., 2011). These natural effects can be intensified by anthropogenic influences as deforestation for agricultural utilization (Aucelli et al., 2012) or the major changes e.g. by mining (Novotny, 2003). As mining sites in hilly or mountainous regions can show steep and due to a recultivation mostly anthropogenic created slopes consisting of e.g. heavy metal polluted sediments (e.g. spoil) with harsh conditions for vegetation, they are often

NHESSD
3, 6271–6319, 2015

prone to erosion processes especially by overland flow induced by heavy rainfall. As those landscapes can act as source for heavy metal pollutants (Servida et al., 2009; Benvenuti et al., 1999), the investigation of the geomorphic process dynamic on such slopes is of major importance for society, as they can show the success of the recultivation projects. Beside the societal relevance, anthropogenic formed landscapes are interesting objects for studies of geomorphic processes. As recultivated landscape were "set back", geomorphic processes start at "time zero" and can be analysed ab initio.

The investigation of fluvial erosion on hilly or mountainous slopes in Mediterranean regions was often done by using "analogue" methods like erosion pins or sediment traps (Della Seta et al., 2009; Haas et al., 2011; Clarke and Rendell, 2006) which are often hard to use and error prone, as their use can lead to influences on the investigated slopes (Haas et al., 2011). Moreover the spatial and temporal resolution of these methods is normally very limited with consequences for the interpretation of the results (Haas et al., 2011). "Digital" geodetic methods like Terrestrial Laserscanning (TLS) also known as Ground-based LiDAR and digital photogrammetry by UAV are increasingly used for geoscientific research (c.f. Abellan et al., 2009; Schürch et al., 2011; Haas et al., 2012; d'Oleire-Oltmanns et al., 2012; Ouédraogo et al., 2014; Peter et al., 2014) and also for the measurement of fluvial erosion or gullying on slopes of the Mediterranean region (Haas et al., 2011; d'Oleire-Oltmanns et al., 2012; Peter et al., 2014; Neugirg et al., 2014). Many of the studies include investigations about the accuracy of the single methods (Ouédraogo et al., 2014; James and Robson, 2012; Fonstad et al., 2013; Kaiser et al., 2014) but there are only less studies that compare UAV and TLS to each other in the means of accuracy (Eltner et al., 2015; Flener et al., 2013; Sperlich et al., 2014) and none that investigate the potential of both methods (especially UAV) for the detection of geomorphic processes in a natural environment by using long time multitemporal data.

Thus the presented work in this study focuses on the use of the methods TLS and digital photogrammetry by UAV photographs to quantify and to analyze the geomorphic

NHESSD
3, 6271–6319, 2015

process dynamic on an artificial steep an sparely vegetated slope of a former iron ore mine on the Mediterranean island Elba/Italy over 5 1/2 years. Beside the quantification and analysis of the erosion processes an additional focus was set on the comparison of both methods and the identification of their potential and limitations for long time monitoring of surface change by geomorphic activity in a pseudo natural environment.

2 Study area

The studied slope is part of the former iron ore mine rio albano (haematite and pyrite) close to Rio Marina and Cavo on the East coast of the Island of Elba, which is located close to the western coast of Italy (see Fig. 1). Elba is known as one of the most important mining sites of Italy, but the iron exploitation at Rio Marina has ceased in 1981 (Servida et al., 2009) by leaving many waste dumps, that are prone to erosion and therefore act as a potential source of heavy metal pollutants (Benvenuti et al., 1999; Mascaro et al., 2001). Especially the topographic structure of the mine with steep, unconsolidated and thus erosion prone slopes in a short distance to the coast (polluted water is flowing directly into the sea) or to infrastructure (main roads) led to a variety of restoration projects on these waste dumps in order to minimize or stop the export of harmful substances (Servida et al., 2009) and sediment.

Figure 2 indicates that the Mine surface is not or only barely vegetated, which is a consequence of the heavy metal concentration of the sediment and the very acid soil and soil water conditions. Servida et al. (2009) measured ph values of 2.08 to 3.35 and very high heavy metal concentrations (e.g. 903.16 $mg\,l^{-1}$ for Fe). This is a decisive disadvantage for any restoration attempts by e.g. reforestation. As a stabilisation of the slope by vegetation is not feasible, the slope was artificially benched in 2002 in order to reduce the flow velocities in order to minimize the erosion by water. Additionally, several artificial barriers were put directly on the slope for erosion control (Fig. 2b), but many of them were swept away by erosion processes during the last years.

NHESSD
3, 6271–6319, 2015

The overland flow from the single short slopes is collected by constructed channels at the foot of the slopes, which drain to a main drainage channel (Fig. 2c). On the end of the constructed channel, a low channel slope gradient makes for a deposition of the transported sediments in a reservoir before the water leaves the mine.

The mainly southernly exposed slopes has an extension of 13 800 m^2 (including 1100 m^2 accumulation area) and consist of mainly coarse-grained (> sand) mine filling material and slag. The slope angles lie between 14 and 69° with a mean of 39° .

The climatic conditions of the region are characterised by a mean annual rainfall of around 750 mm (for Populonia, which is located on the Italian mainland close to Elba) with main precipitation occurring during the winter period (83 % of rainfall between September and April) and a mean annual temperature of 15.3 °C (Giusti, 1993).

3 Materials and methods

3.1 Field campaigns and data acquisition

The investigation started in September 2009 during a field course with students with the first scanning of the whole slope. Since 2009 four more scanning campaigns followed between April 2012 and April 2015 in order to quantify the erosion processes and are now additionally embedded in a DFG founded project (German Science Foundation/HA 5741/3-1 and SCHM 1373/8-1). As the scanning of the very complex slope is very time consuming and in order to test the applicability of digital photogrammetry by UAV photographs, the slope was additionally surveyed with aerial photographs by an UAV during two campaigns in April 2013 and April 2015. The methodological background of both, TLS and digital photogrammetry as well as the comparison of both methods on the base of the data is described in detail within the next sections.

NHESSD
3, 6271–6319, 2015

3.1.1 Terrestrial laser scanning

Terrestrial laser scan data was acquired using the Riegl LMS Z420i scanner (http://www.riegl.com), which has a maximum measurement range up to 1000 m, an accuracy of 0.01 m (distance by single shot) and a scanning rate of up to 8000 pts s^{-1}. The scanner uses a near infrared laser signal by a beam divergence of 0.25 mrad, which means an increase of the laser footprint by 0.0025 m per 100 m. A mounted digital SLR camera (Nikon D700 with a 20 mm lens) takes referenced high resolution pictures of the scanned objects, in order to define the color (RGB value) of every single point of the LiDAR point cloud. These colour information are applicable for a manual or automatic filtering of vegetation (Haas et al., 2011). The scanner and the SLR camera are operated by an external PC and the scanner software RiscanPro.

The mine was scanned from between 7 (2009) to 11 (2012) different scan positions (Table 1) in order to minimize shadowing effects. The angular scanning resolution was set to 0.05° (x and y direction). Figure 2a shows as an example the location of the single scan positions of the 2013 campaign. For an accurate referencing of the point clouds six fixed and stable tie points were installed on or near the slopes (reflector disks with a diameter of 0.1 m). These were mounted with screws or nails on the wooden debris flow barrier (see Fig. 3). The global coordinates of these tie points were measured using a differential GPS and a total station (3.2).

Following the data acquisition in the field, the software Riscan Pro (3-D scanner software) was used for the postprocessing of the raw data. The single point clouds of each time step were registered globally using the scanned tie points. All scan positions of each single scanning epoch were referenced to one “master scan” which provided these global coordinates. All other scan positions were well distributed over the slope in order to ensure enough overlap of the single point clouds for the following referencing procedure using an ICP-based algorithm (MSA tool in Riscan Pro). The values for the referencing accuracy lie between 0.007 and 0.013 m. Table 1 shows the number of

NHESSD
3, 6271–6319, 2015

the scan positions on the slope, the referencing accuracy as mean value, the resulting number of points and the point density (points m^{-2}) for every single epoch.

After these processing steps in Riscan Pro the resulting raw point clouds were ASCII formatted (x, y, z, RGB values) and exported as global coordinates. All further processing steps (e.g. filtering of vegetation, DEM generation) were done by using LIS Desktop/SAGA GIS (3.2).

3.1.2 UAV survey – photogrammetry

During the campaign in April 2013 and April 2015 the Rio Marina mining area was additionally monitored by using an UAV (Falcon 8 octocopter by Astec Ascending technologies, Fig. 4) with a mounted and calibrated Sony camera Nex 5 (internal orientation is known and was used for the processing, resolution 14 Megapixel). The system comes with a remote control and an auto pilot system (altimeter, GPS, inclination sensors, gravity sensor) and can be operated both manually by the remote control and automatically using an external PC and a flight plan. Due to the very complex topography of the slope and very windy conditions during the flights, the UAV was in both cases operated manually by the pilot without using a flight plan (mean flight height: 50–80 m over ground). Table 2 shows the important values for the two flight campaigns. During the flights a sum of 48 to 158 pictures with an overlapping of at least 60 % were taken. For the producing of orthophotos and 3-D point clouds of the area an exterior orientation was necessary (Lindner, 2009). Thus a sum of 31 to 37 "true ground points" (red crosses in the case of the 2013 campaign and red carpets with a reflector in the centre for the 2015 campaign) were distributed over the slope (Fig. 4) and measured in the field by using a differential GNSS antenna. In order to adjust all GCP's in one common and stable global coordinate system (UTM 32N ETRS 89 with ellipsoidal heights/EPSG:25832), during the 2015 campaign one fix point was measured with a Stonex S9III GNSS antenna by using RTK information (RTK Fix by NTRIP) from an Italian service (Topcon positioning/GeoNRTK by Geotop Italia – www.geotop.it). Due to the unstable availability of the mobile network, this fixed point

NHESSD
3, 6271–6319, 2015

was used as base position for a rover-base system (Leica GS09 differential GNSS antenna with radio transmission of an own correction solution). Using this system in combination with a Totalstation (Leica TPS 1205) all GCP's and the TLS reflectors (see Fig. 3) of the 2015 campaign were measured with a 3-D accuracy below 3 cm. As the RTK information were only available during the 2015 campaign, the 2013 GCP's were adjusted to the 2015 coordinate system by using the 2015 coordinates of TLS reflectors as control points and Leica GeoOffice to shift them (module shift). The comparison of the coordinates of the 2 campaigns shows a mean deviation below 0.05 m (for details see Table 2).

In order to produce ortho-images and photogrammetric derived point clouds, the raw data (photographs and GCP) were processed by using the software PHOTOSCAN PROFESSIONAL (Agisoft). The accuracy of the exterior orientation (by GCP) of the single campaigns shows a mean deviation of 0.034 to 0.048 m (Table 2).

The resulting dense point clouds were ASCII formatted (x, y, z and RGB values) and exported in order to use LIS Desktop/SAGA GIS for the following processing steps (3.2). The referenced orthophotographs (UTM 32N ETRS 89 EPSG:25832) were exported as referenced TIF-files with a ground resolution of 0.05 m for all epochs. These pictures were afterwards used for visualisation and for a visual interpretation/validation of the results.

3.2 Processing of the raw point clouds, DEM derivation and spatial analysis

After the export of the raw point clouds from Riscan Pro (TLS data) and Photoscan Professional (photogrammetric data), the globally registered point clouds have to pass several processing steps in the LIS/SAGA GIS environment (LIS desktop and LIS workstation). In order to compare both kind of data, the workflow is identical for both the TLS and the photogrammetric data (Fig. 5), excluding the value overlapping, which was only derived for the photogrammetric data.

The point clouds (x, y, z coordinates and the RGB values) were imported into the database of LIS (http://www.laserdata.at) and all following processing and analyzing

NHESSD
3, 6271–6319, 2015

steps were conducted. These steps can be separated in point cloud thinning, vegetation filtering, filtering by the value overlapping (only UAV data), a final filtering step, DEM generation and estimation of errors:

Point cloud thinning

- Positive and negative outlier measurements were removed automatically by a filter based on the elevation variability of points in a specified point neigbourhood (this was in fact only necessary for the TLS data set).
- All point clouds were clipped to the manually mapped extent (polygon) of the area of interest (AOI) in order to reduce processing time for the following steps and exclude the dense vegetation (trees and shrub) around (see Fig. 2).
- The point clouds were filtered in 2-D blocks to reduce redundant points representing overrepresented surfaces close to the scanner. This step reduced the maximum point density of the TLS data to 625 pts m^{-2} and led to a reduction of their point numbers by up to 60 % depending on the data set.

Vegetation filtering

- For vegetation filtering, a two-step procedure was then conducted. The RGB values provided by the SLR camera of the scanner or the photogrammetric data for each measurement points were converted to HSV color space, which made a deletion of all green hued points (as by us supposed to represent vegetation) possible. As quite some vegetation visible on the mine slope is either gray or light red colored (especially dead vegetation) this was not successful in removing all vegetation points.
- A region growing algorithm preceded by a parameter controlled segmentation algorithm and a rule based classifier were then applied to split the dataset

NHESSD
3, 6271–6319, 2015

in ground and non-ground points (cf. Ying Yang and Förstner, 2010; Bremer et al., 2013).

Including the parameter overlapping (this was in fact only necessary for the photogrammetric point cloud!)

- The overlapping values (as sum values for the single zones) were included by a reclassification of the colorized (RGB values) overlapping map, that was exported as TIF-file from the Photoscan Professional Report (only available as pdf-file). The TIF-file was referenced on the base of the UAV coordinates (which were exported as x, y coordinates) using ESRI ArcMap. The produced Geo-Tif was then imported to SAGA GIS where the RGB values (as value for the amount of overlapping) were assigned as additional attributes to the filtered point cloud. Using the RGB information the H values (Hue value of the HSV color model) for every single point of the point cloud were derived and also added to the filtered point cloud. By a reclassification of the H values the number of overlapping could added to every single point of the point cloud. On the base of this value the AoI of the UAV data was derived for points with an overlapping of at least 8. As AoI of the TLS data and the UAV data are different, the comparison of both methods was done on the base of the UAV AoI.

Final filtering step

- In order to produce consistent data sets, a raster data set of all single epochs (UAV and TLS) was produced, which provides the information of vegetation (as no data value) or true ground (value 1). These raster data sets were multiplied in order to produce one final filtering mask with no data areas (vegetation) and true ground information (value 1). All following analyzing steps are then based on a consistent filtering result.

NHESSD
3, 6271–6319, 2015

DEM generation and spatial analysis

- The resulting ground points were then used for the construction of a 0.2 m digital elevation model. Gridding was achieved by using a moving plane approach taking the elevation value of plane fit to the 12 nearest neighbours within a 0.1 m search radius to the cell center. As the gridding method of moving planes can result in artefact next to no-data areas, the no-data areas were enlarged by two lines of cells after the gridding procedure to remove these artefacts.

- The spatial analysis was done within the framework of SAGA GIS (version 2.2.0) by using the integrated terrain analysis tools. In order to analyse the geomorphic changes on the slope during the 5 1/2 years time period, we used the stream power index (Moore et al., 1999) for three single epochs (2009, 2013 and 2015) as proxy for the exposure to fluvial erosion:

$$SPI = SCA \tan(slope) \quad (1)$$

  Where SPI is the stream power index, SCA is the specific sediment contributing area (Quinn et al., 1991) and the slope was derived after Zevenbergen and Thorne (1987).

Evaluation of the error

- To estimate the error of the TLS and the photogrammetric data, an approach of Wheaton et al. (2010) was conducted. As this approach is crucial for the sediment balancing, it is described in detail within the following section.

3.3 Sediment balancing

The final DEMs of each time step were then used for the volume balancing. As all point surveys contain measurement errors and spatially variable variations that need

NHESSD
3, 6271–6319, 2015

to be accounted for when using the data for measuring surface changes or for volume estimations, those errors are propagated into the DEMs of each time step during the gridding process and accumulate when two DEMs are used for the purpose of height differencing or volume balancing. For a quantification of the error in DEM values, we adapt a statistical approach and assume that the errors of the grid cells are normally distributed with a mean of zero and that the overall DEM error can be expressed by a standard deviation (Brasington et al., 2000). The error of each DEM can then be propagated into the DEM of Difference ("DoD") using the following simple equation (Brasington et al., 2000).

$$\delta_{\mathrm{DoD}} = \sqrt{\sigma^2_{\mathrm{DEM1}} + \sigma^2_{\mathrm{DEM2}}} \tag{2}$$

Using this approach, independence of both DEMs is assumed, which yields to optimistic (i.e. low) values of δ_{DoD} (sometimes also termed "simple Level of Detection", LoD). We therefore follow Burrough and MacDonnell (1998) in considering the correlation between two elevation models.

$$\delta_{\mathrm{DoD}} = \sqrt{\sigma^2_{\mathrm{DEM1}} + \sigma^2_{\mathrm{DEM2}} + 2\sigma_{\mathrm{DEM1}}\sigma_{\mathrm{DEM2}}r_{\mathrm{DEM1DEM2}}} \tag{3}$$

The absolute value of each grid cell in the DoD is then related to δ_{DoD} to calculate a t score.

$$t = \frac{|Z_{\mathrm{DEM2}} - Z_{\mathrm{DEM1}}|}{\delta_{\mathrm{DoD}}} \tag{4}$$

In following Wheaton et al. (2010), we apply a simple probabilistic thresholding at the 95 % confidence interval to classify DoD cells as probably representing real change or measurement error. Only the cells classified as displaying real change are used for budget calculation. The spatially uniform height difference error δ_{DoD} can be used to arrive at an estimate of the total volumetric error of all n raster cells with cell size c in

NHESSD
3, 6271–6319, 2015

the Dod (Lane et al., 2003).

$$\delta_{\mathrm{Dod}}\sqrt{n}c^2 \tag{5}$$

The errors of the individual DEMs can be estimated via comparing two different measurements between which the observed surface has not changed or by using stable areas (Westaway et al., 2000). As repeat measurements would have been to time consuming for both TLS and UAV for this study, stable areas were used for calculating the LoD. These areas are distributed over the whole slope (Fig. 8a) and we assume that no surface changes occur on these areas during the single epochs. Therefore all detected changes can be seen as error. Based on those errors, the resulting δ_{Dod} was then applied to the budgeting process of each TLS and UAV epoch. All values of the standard deviations (σ) for each TLS/UAV period and the corresponding LoDs can be found in Table 3.

3.4 Comparison of TLS and UAV data

The comparison of the TLS and UAV data was done in two different ways:

DEM to DEM comparison

- Using the 2013 and 2015 Data, the UAV-DEMs and the TLS-DEMs were compared based on the smaller AoI of the UAV data. This was done on the base of a 0.2 m DEM resolution and using the module Cut and Fill of Heckmann (2006) after the work of Lane et al. (2003) in SAGA. The resulting difference grid and the derived volumes (including the single LoD) could be used for the following quantitative and qualitative analyzing steps.

Comparison of the sediment balancing

- The results of the sediment balancing of the TLS and the UAV data for the 2013 to 2015 epoch were compared. The result was also used for quantitative and qualitative analyzing.

NHESSD
3, 6271–6319, 2015

4 Results and discussion

4.1 Quantification of surface changes by TLS data

The TLS repeat measurements yielded a LoD between 0.036 and 0.100 m (Table 3) for the single epochs. Thus the volumetric surface changes in Table 4 comprise only surface changes over the respective LoDs. The overall balance for the 2009 to 2015 epoch was not derived by summing up the values of the single epochs but by using only the 2009 and 2015 DEMs. As between the single epochs surface changes may vary from erosion to accumulation, the sum of the single epochs and the comparison of the 2009 to 2015 epoch differ clearly.

As there are volumetric changes of $-188.28\,m^3$ (erosion) and $+191.54\,m^3$ (accumulation) for the epoch 2009 to 2015 detectable, the sediment balance seems to bee even or slightly positive. As expected most of the erosion takes place on the slope and the accumulation is concentrated in the reservoir (Fig. 6).

Erosion on the slopes can be separated in areas with sheet erosion and areas that show rill erosion or erosion in channels and sums up to a value of $-134.61\,m^3$. The pattern of erosion is comprehensible from a geomorphic point of view, but shows a few inconsistencies, which are exemplary highlighted in Fig. 6b and c. Figure 6b and d shows two examples (more of them are visible all over the AoI) for the missing information due to shadowing effects in areas with a complex topography, which is the case in and around the constructed channel and in the incised gullies and channels (and of course in the areas with vegetation, which are not highlighted!). This missing information, especially in the gully, probably leads to an underestimation of the erosion on the slopes. Beside this, Fig. 6c shows sheet erosion on the top of the slope with the missing of a down slope connection. This surface changes are in fact not the result of erosion by water but the consequence of a subsidence in this area, which could be verified in the field. Thus this surface change should strictly not be applied to the volumetric changes by fluvial erosion (in fact it was excluded from the volumetric balancing!).

NHESSD
3, 6271–6319, 2015

Most of the accumulation in the AoI is concentrated on the flat surfaces as e.g. on the terrace over the gully in Fig. 6d and on a slope in the eastern part of the AoI. The accumulation on the terrace is the consequence of a shifting of the channel during a high precipitation event on this terrace and a displacement of the gully system from west to east (for detail see Sect. 4.2). The accumulated material is delivered from the small channel on the bottom of the slope and a small upstream gully, which is not detectable by the TLS data, but by the UAV data (see Sect. 4.2). The accumulation on the western slope is also caused by a heavy rainfall event, where water and material was transported over the terrace (which is outside the AoI) onto the slope. Traces of this overflow could be verified in the field.

But most of the accumulation within the AoI took place on the surface of the reservoir. The pattern of accumulation is also comprehensible from a geomorphic point of view and is the consequence of high discharge events between 2009 and 2015 (Fig. 9). Taking only into account the 2009 to 2015 epoch, the surface changes in the reservoir are predominantly positive and show only accumulation, which indicates that the reservoir acts as a sediment sink. Both the sediment balancing in Table 4 and the surface changes in Fig. 7 for all single epochs show, that there is not only accumulation but also erosion present in the reservoir. Thus the reservoir can be seen as a sediment sink as well as a sediment source and as a consequence it seems that sediment leaves the AoI during events with higher runoff. As on the slopes there are also areas affected by shadowing effects. One of those is highlighted in Fig. 6e and shows an area with no data under and behind a shrub (see also Fig. 4b). These no data areas can also lead to an underestimation of the volume balancing.

Summing up the discussed results of the TLS data, the positive sediment balance seems to be unrealistic, especially in the context of erosion and probable through transport of material on the surface of the reservoir. This fact indicates the transport of material out of the AoI and thus the sediment balancing had to be expected as clearly negative. The reasons for the even or slight positive sediment balance are:

NHESSD
3, 6271–6319, 2015

- A clear underestimation of erosion on the slopes because of (i) no data values beneath vegetation on the eastern part of the slope and (ii) because of shadowing effects due to a very complex surface topography. Especially the complex gully structure in Fig. 6d lead to a loss of information in an area with heavy erosion. Beside this (iii) the level of detection varied between the single epochs and the 2009 to 2015 epoch. Slight erosion processes (e.g. erosion by sheet flow) are only detectable if they have a magnitude over the LoD. While the surface changes in the reservoir is limited on the narrow reservoir, which leads to surface changes over the LoD, it can therefore be assumed, that especially erosion by sheet flow on the slope is underestimated in the sediment balancing.

- The accumulation in the reservoir seems to be well represented, but Table 4 and Fig. 7 show, that there are also uncertainties due to the alternation of erosion and accumulation. This probably leads to an overestimation of the accumulated material for the 2009–2015 epoche in contrast to the sum of the single epochs.

- An important factor in comparing sediment sources and sediment sinks is the different bulk density of source material and accumulated material. As source material normally has a higher bulk density, fluvial accumulated material normally is less dense, which probably leads to a difference in the calculated volumes based on measured surface changes.

A few of the described problems are the consequence of the unfavorable viewing angle of TLS especially on surfaces with a complex topography. To investigate if a bird eye view can minimize the effects of shadowed areas, a volume balancing by an UAV based digital photogrammetry was conducted.

4.2 Quantification of surface changes by UAV data

As the TLS data, the UAV data show also a consistent pattern of surface changes within the AOI for the 2013 to 2015 epoch (Fig. 8). The highlighted areas in Fig. 8c show,

NHESSD
3, 6271–6319, 2015

that surface changes are very well detectable even within the very complex surface topography around the constructed channel (Fig. 8c red) and that vegetation is quite well filtered by the used filtering workflow (Fig. 8c green). Figure 8c (blue) shows an artificial surface change due to the presence (2015) and absence (2013) of the UAV transport box and back packs of the investigators. This can be used for the evaluation of the accuracy of the measured surface changes, as the volume of the transport box is well known. The measured artificial surface changes by the DoD fit quite well to the known box dimensions. (difference of $\sim 10\,\%$).

The surface changes on the AoI can be separated in three major parts: (i) fluvial rill erosion by concentrated flow on the steep slopes is only slight with no visible accumulation on the corresponding flat areas between the slopes. (ii) Surface changes on the eastern part of the middle slope and on the whole lower slope are indicating intensive gullying by concentrated flow. These gullies belong to one channel system that has its origin on the topmost terrace outside of the AOI (Fig. 2a). As a consequence of the increasing catchment size and due to the already described shifting of the channel system, the "gully complex" on the lower slope consists of three single gullies, with the highest surface changes at the eastern gully (deepening of up to 2.4 m). These very high erosion rates can be seen as a consequence of very heavy rainfalls events between April 2013 and April 2015. Precipitation data of the Vecchia Aurelia meteo station (Fig. 9) show for this region three rainfall events higher than 50 mm in winter 2013/14 and two in autumn/winter 2014/15 with the highest one in October 2014 ($95.2\,\mathrm{mm\,d^{-1}}$). (iii) The flat embanked area (sediment reservoir) on the bottom of the slopes shows both, zones of accumulation and erosion. While the central part is dominated by accumulated material, the western part shows linear erosion, starting at the eastern gully on the described lower slope. The pattern of accumulation as well as erosion is clearly visible on the DoD and on the aerial photographs and show a braided river system, including lateral erosion on the western dam. This fact indicates transport of material out of the AOI. This through transport of material at the sediment reservoir and the good resolution of the erosion within the gullies explains the clearly negative

NHESSD
3, 6271–6319, 2015

sediment budget of −43.21 m^3 (Table 5). In fact this value must be seen as a minimum value, as the AOI does not include the upper slopes of the mine.

Summing up the discussed results of the UAV data, the negative sediment balance seems to be realistic, but while the heavy erosion in the gullies is well detected, the erosion on the slopes is probably underestimated. Especially in the context of the high LoD of 0.108 m, erosion on the slopes by sheet flow or the erosion in small rills must be seen as not detectable by this special investigation design, as from a geomorphic point of view such erosion should have taken place on the slopes but is not expected to exceed the value of the LoD (> 0.108 m).

4.3 Analysis of the geomorphic changes by using the stream power index

Figure 10a shows the changes of the stream power index (SPI), as proxy for the erosion potential, between 2009 and 2015 for the whole slope. It is evident from this that, the geomorphic processes (especially fluvial erosion) lead not only to the already discussed high amounts of erosion and deposition, but also to changes in the hydrological conditions. These changes can also be seen in the distribution of the SPI (Fig. 11). While the mean logarithmised SPI values (SPI is log normal distributed) show only a slight switch of the SPI from −0.252 to −0.309, the maximum value increased from 3.249 to 3.489. This slight shifting is the consequence of an ongoing back-cutting of the hillslope channels up to the flat terrace (Fig. 10b). This corresponds with an enlargement of their hydrological catchment (increasing values of the SPI at the channel heads) and first indications of a beginning dissection of the terrace (arrows in Fig. 10b). From a prognostic point of view it is to be expected, that this dissection will proceed in the future with a following destruction of the terrace and a coupling of the two bordering slopes.

Such a dissection of a terrace and a coupling of two slopes can already be found at the lowest one (Fig. 10c). The flow paths of the channels already shifted from the west to the east with a consequent coupling of slope sections and steepening of the channel

NHESSD
3, 6271–6319, 2015

slopes, indicated by the increasing SPI. This fits very well to the massive erosion in the gully structures and the enlargement of the hydrological catchments. While the western gully was still present in 2009 the first eastwards shifting (to channel 2 in Fig. 10c) of the flow parts occurred between 2009 and 2013, probably during high intensity rainfall events (see Fig. 9; 6 rainfall events over 50 mm d^{-1} were recorded during this period). Between 2013 and 2015 the shifting continued to the eastern-most channel (channel 3 in Fig. 10c), with the highest erosion amounts between 2014 and 2015 (indicated by the TLS data and the very high rainfall intensities in this period, Fig. 9). Due to the intensive gullying and the back-cutting of this channel, it seems that the channel is now fixed to this position, with a high erosion potential (indicated by the SPI). It can be expected, that this will lead to an ongoing dissection of the bordering terrace and to a following deactivation of the western channels (channel 1 and 2 in Fig. 10c).

As the results of the UAV and the TLS data in Sect. 4.2 differ visibly and DEMs of both, UAV and TLS data had to be used for the spatial analysis in Sect. 4.3, TLS and UAV data sets were compared in detail. The result of the analysis is described within the next section.

4.4 Comparison of TLS and UAV data

4.4.1 Comparison of the resolution

The comparison of the point densities of the filtered point clouds of the 2013 UAV and TLS data (the 2015 data provide similar results) show considerable differences (Fig. 12). While the maximum values of the TLS data are much higher (but with a large scattering, Table 1), the UAV data are much more homogenous with a low scattering.

TLS data

– The high densities of the TLS data can be found at overlapping areas (overlapping of scans of one or more scan positions) and at the regions close to the scan

NHESSD
3, 6271–6319, 2015

positions, which is the consequence of the adjustable angle resolution. During the scanning campaigns an angle resolution of 0.05° was used. Thus the distances between the measured points are smaller at regions close to the scanner and vice versa.

– Low densities of the TLS data are distributed over the slope and are the consequence of shadowing effects, vegetation cover, unfavourable incidence angles of the laser signal (especially at flat areas) and areas with less scan positions.

UAV data

– The UAV data show a lower maximum of the point density, but the distribution is very homogenous. Thus the mean point densities are higher than all the TLS point densities of the single epochs (Table 1).

– The mean values of the 2013 and 2015 data are identical although the data are based on a very different amount of pictures (Table 1).

– Point density is also constant on areas with a complex surface topography, which is the consequence of the birds eye view with shadowing effects only beneath vegetation.

– As a consequence of the filtering process, areas with vegetation cover provide only low point densities. As the UAV records the AoI from the birds eye view, there are no ground points left after the filtering procedure. This effect is the stronger the denser the vegetation is, especially at shrubs that can be found in the spare vegetation areas. Thus now surface information can be provided for these areas by the UAV data.

– Low point densities can also be found at areas with a very homogenous surface structure (light coloured and very smooth surface, arrow in Fig. 12). Obviously the

NHESSD
3, 6271–6319, 2015

SfM algorithm has problems to detect similar points in both the 2013 and the 2015 pictures.

The different point density, the different distribution and the differences in the LoDs lead to differences in the surface changes and the calculated volume balancing, which is presented and discussed within the next section.

4.4.2 Comparison of the sediment balancing

As mentioned above, the result of the volume balancing of the TLS and the UAV data varied strongly. Table 6 shows, that while the TLS based volume balancing results in a positive balance, the balance of the UAV data is clearly negative. These differences are the consequence of both an underestimation of the erosion on the slopes by the TLS data and an underestimation of the accumulation in the reservoir by the UAV data. Both effects are also clearly visible in Fig. 13.

- Due to the above mentioned shadowing effects, the erosion within the incised gullies or around the constructed channel is not detectable by TLS with the used investigation design (location of the scan positions). Due to the birds eye view of the UAV, surface changes in the complex areas are very well detected and do not show data holes within those regions.
- Surface changes within the reservoir are much better detected by the TLS data (except the undercutting of the eastern dam). While the pattern of the accumulation area is very similar between UAV and TLS data, there are also very low surface changes identified in the TLS data, which show no surface changes in the UAV data. This is probably the consequence of the higher LoD of the UAV data (Table 3), as only surface changes over 0.108 m are identified as significant surface changes.

As the visual comparison of the TLS and UAV data in Fig. 12 only shows the differences between the no-data values and the measured surface changes, Fig. 13

NHESSD
3, 6271–6319, 2015

provides information about the comparison of the surface changes that are detected as surface changes in both datasets. It is clearly visible, that there is no systematic error (e.g. because of a shifting of one dataset) detectable as e.g. James and Robson (2014) described for their UAV data (bowl effect). The bowl effect could probably be minimized in this study by distributing the GCPs also close to the borders of the investigated slope, by using the factor overlapping in order to generate a stable geometry and by using the values of the internal orientation of the camera. The R^2 of the correlation of the TLS and the UAV data shows a value of 0.791 ($p < 0.0001$). Nevertheless the scattering is partly high in an area where the amounts of erosion are quite lower in the TLS data (arrow 1 in Fig. 14). These points are located on or close to the border areas of the main gully on the lower slope and are an effect of the gridding of the point clouds to derive the DEMs. While the point densities of the UAV data are very homogenous in the main gully, there are no TLS point data available inside the gully. Especially in the border areas there are only less TLS data (and in fact no data of the inner slopes of the gully) available for the DEM generation, which leads to higher surface values in contrast to the UAV data. Despite the enlargement of no-data areas during the DEM generation process (3.2), this effect could not be completely eliminated.

5 Conclusions

The presented investigations show, that both UAV and TLS data are suitable methods to detect surface changes on steep slopes and that there is a great potential to quantify and analyze geomorphic processes with a high level of detail. Due to the high temporal, but especially the high spatial resolution, these methods offer new perspective for the geomorphic process analysis. Beside the potential of the methods, limitations were detected, which have to be taken into account for the interpretation of the results and the use of the data for statistical analyses, modelling and of course for further investigations.

NHESSD
3, 6271–6319, 2015

While TLS offers much better accuracies (LoDs), there exist problems with inhomogenous point densities and data holes in shadowed areas. These effects could be minimized by scanning the surface from more than the used scan positions. This would eliminate both shadowing effects and inhomogenous point densities. But it is needless to say that to capture the complex surface of the mine would lead to a much longer stay in the field.

In contrast digital photogrammetry by UAV photographs offers new perspectives for monitoring geomorphic processes in a complex environment with a quick workflow in the field (in this case ∼ 4 h for the slope in contrast to the 2 days for TLS acquisition). Due to the birds eye view shadowing effects of e.g. incised gullies do not appear and the intensive gullying is quite well detectable. The disadvantages of the method are the missing data under lower vegetation (e.g. shrub or higher grass), the problems of very homogenous surface conditions (color, contrast) and the high LoDs in this study. As the high LoD makes it difficult to investigate processes with low magnitudes and processes over shorter time steps (e.g. single events), the LoD should be minimized. Probably this goal could be achieved by a lower flight altitude, which normally would lead to a higher resolution of the pictures. If this will lead to a lower LoD should be analyzed during further investigations.

Summing it up for the study design in this work, both methods show the pattern and the amount of erosion and accumulation of geomorphic processes with magnitudes over the respective LoDs quite well, which can sustain important information about the geomorphic process dynamic on such slopes. While processes with high magnitudes (e.g. gullying) are detectable due to high amounts of surface changes even over short monitoring periods, geomorphic processes which cause only slight surface changes are only detectable over longer time intervals. But as geomorphic processes can overlap in time and space, and the probability increases with time, short monitoring periods are urgently required to distinguish single geomorphic processes (e.g. sheet erosion, rill erosion) and for example bring them together with e.g. single precipitation events. Therefore future investigations should focus on the opportunities to reduce the

NHESSD
3, 6271–6319, 2015

LoD of both TLS and UAV data or on the potential and the limitations of a combination of both methods.

Beside the methodological aspects this study showed, that the recultivation of the mine must be seen as not sustainable as severe erosion takes place all over the slope. Most of the artificial structures are now dysfunctional or have already been 7 years after the recultivation at the beginning of the monitoring in 2009. The dominating geomorphic processes are obviously fluvial processes (beside the singular subsidence), indicated by the intensive gullying and (based on the UAV data) the lateral erosion along the constructed channel. As the analysis of the SPI showed, this fluvial geomorphic activity leads to a massive change of the hydrological conditions, with increasing catchment sizes and shortened and steepened flow paths.

While reforestation is not feasible due to the very acid conditions, the artificial slope topography and the artificial structures need an adaption with a following regular inspection and maintenance to control surface runoff. Failing which, the slope will become an erosional landscape as it was before the recultivation, including the risk exposure for the adjacent environment (harmfull substances) and infrastructure (e.g. by debris flows).

Acknowledgements. As the data were collected during field courses with students for many years, many "student generations" were involved in their acquisition. They are gratefully acknowledged by the authors. The processing of the data was done within the framework of the DFG (German science foundation) project Questar^{3D} (grant numbers: HA 5740/3-1 and SCHM 1373/8-1).

NHESSD
3, 6271–6319, 2015

References

Abellán, A., Jaboyedoff, M., Oppikofer, T., and Vilaplana, J. M.: Detection of millimetric deformation using a terrestrial laser scanner: experiment and application to a rockfall event, Nat. Hazards Earth Syst., 9, 365–372, 2009.

Aucelli, P. P. C., Conforti, M., Della Seta, M., Del Monte, M., D'uva, L., Rosskopf, C. M., and Vergari, F.: Quantitative assessment of soil erosion rates: results from direct monitoring and digital photogrammetric analysis on the Landola catchment in the Upper Orcia Valley (Tuscany, Italy), Rend. Online Soc. Geol. It., 21, 1199–1201, 2012.

Auerswald, K., Fiener, P., and Dikau, R.: Rates of sheet and rill erosion in Germany – a meta-analysis, Geomorphology, 111, 182–193, 2000.

Benvenuti, M., Mascaro, I., Corsini, F., Costagliola, P., Parrini, P., Lattanzi, P., and Tanelli, G.: Environmental problems related to sulfide mining in Tuscany, Chronique de la Recherche Minière, 534, 29–45, 1999.

Brasington, J., Rumsby, B. T., and McVey, R. A.: Monitoring and modelling morphological change in a braided gravel-bed river using high resolution GPS-based survey, Earth Surf. Proc. Land., 25, 973–990, 2000.

Bremer, M., Rutzinger, M., and Wichmann, V.: Derivation of tree skeletons and error assessment using LiDAR point cloud data of varying quality, ISPRS J. Photogramm., 80, 39–50, 2013.

Bryan, R. B.: Soil erodibility and processes of water erosion on hillslope, Geomorphology, 32, 385–415, 2000.

Burrough, P. A. and MacDonnell, R. A.: Principles of Geographical Information Systems, 1st edn., Spatial information systems, Oxford University Press, Oxford, 1998.

Clarke, M. L. and Rendell, H. M.: Process-form relationships in Southern Italian badlands: erosion rates and implications for landform evolution, Earth Surf. Proc. Land., 31, 15–29, 2006.

Della Seta, M., Del Monte, M., Fredi, P., and Lupia Palmieri, E.: Space–time variability of denudation rates at the catchment and hillslope scales on the Tyrrhenian side of Central Italy, Geomorphology, 107, 161–177, 2009.

Diodato, N. and G. Bellocchi: Assessing and modelling changes in rainfall erosivity at different climate scales, Earth Surf. Proc. Land., 34, 969–980, 2000.

NHESSD
3, 6271–6319, 2015

d'Oleire-Oltmanns, S., Marzolff, I., Peter, K., and Ries, J.: Unmanned aerial vehicle (UAV) for monitoring soil erosion in Morocco, Remote Sensing, 4, 3390–3416, 2012.
Eltner, A., Baumgart, P., Maas, H.-G., and Faust, D.: Multi-temporal UAV data for automatic measurement of rill and interrill erosion on loess soil, Earth Surf. Proc. Land., 40, 741–755, 2015.
Flener, C., Vaaja, M., Jaakkola, A., Krooks, A., Kaartinen, H., Kukko, A., Kasvi, E., Hyyppä, H., and Alho, P.: Seamless mapping of river channels at high resoloution using mobile LiDAR and UAV photography, Remote Sensing, 5, 6382–6407, 2013.
Fonstad, M. A., Dietrich, J. T., Courville, B. C., Jensen, J. L., and Carbonneau, P. E.: Topographic structure from motion: a new development in photogrammetric measurement, Earth Surf. Proc. Land., 38, 421–430, 2013.
Giusti, F.: La Storia Naturale della Toscana Meridionale, Monte dei Paschi di Siena, Italy, 1993.
Haas, F., Heckmann, T., Becht, M., and Cyffka, B.: Ground-based laserscanning – a new method for measuring fluvial erosion on steep slopes, in: Proceedings of the Symposium GRACE, Remote Sensing and Ground-based Methods in Multi-scale Hydrology, Melbourne, Australia, 28 June–7 July 2011, 163–168, 2011.
Haas, F., Heckmann, T., Wichmann, V., and Becht, M.: Runout analysis of a large rockfall in the Dolomites/Italian Alps using LIDAR derived particle sizes and shapes, Earth Surf. Proc. Land., 37, 1444–1455, 2012.
Heckmann, T.: Cut and Fill Module for SAGA GIS 2.2.0, open source GIS module, Eichstaett, 2006.
James, M. R. and Robson, S.: Straightforward reconstruction of 3D surfaces and topography with a camera: accuracy and geoscience application, J. Geophys. Res., 117, F03017, doi:10.1029/2011JF002289, 2012.
James, R. J. and Robson, S.: Mitigating systematic error in topographic models derived from UAV and ground-based image networks, Earth Surf. Proc. Land., 39, 1413–1420, 2014.
Kaiser, A., Neugirg, F., Rock, G., Müller, C., Haas, F., Ries, J., Schmidt, J.: Small-scale surface reconstruction and volume calculation of soil erosion in complex Moroccan gully morphology using structure from motion, Remote Sensing, 6, 7050–7080, 2014.
Lane, S. N., Westaway, R. M., and Murray, H. D.: Estimation of erosion and deposition volumes in a large, gravel-bed, braided river using synoptic remote sensing, Earth Surf. Proc. Land., 28, 249–271, 2003.
Lindner, W.: Digital Photogrammetry – A Practical Course, Springer, Berlin, Heidelberg, 2009.

NHESSD
3, 6271–6319, 2015

Mascaro, I., Benvenuti, M., Corsini, F., Costagliola, P., Lattanzi, P., Parrini, P., and Tanelli, G.: Minewastes at the polymetallic deposit of Fenice Capanne (southern Tuscany, Italy), mineralogy, geochemistry and environmental impact, Environ. Geol., 41, 417–429, 2001.
Moore, I. D., Grayson, R. B., and Ladson, A. R.: Digital terrain modelling: a review of hydrogical, geomorphological, and biological applications, Hydrol. Process., 5, 3–30, 1991.
Neugirg, F., Kaiser, A., Schmidt, J., Becht, M., and F. Haas: Quantification, analysis and modelling of soil erosion on steep slopes using LiDAR and UAV photographs, in: Sediment Dynamics from the Summit to the Sea, Proceedings of a symposium held in New Orleans, Louisiana, USA, 11–14 December 2014, IAHS Publ., 367, 51–58, 2014.
Novotny, V.: Water Quality – Diffuse Pollution and Watershed Management, Hoboken, Wiley, New Jersey, 598 pp., 2003.
Ouédraogo, M. M., Degré, A., Debouche, C., and Lisein, J.: The evaluation of unmanned aerial systems-based photogrammetry and terrestrial laser scanning to generate DEMs of agricultural watersheds, Geomorphology, 214, 339–355, 2014.
Peter, K. D., d'Oleire-Oltmanns, S., Ries, J. B., Marzolff, I., and Ait Hssaine, A.: Soil erosion in gully catchments affected by land-levelling measures in the Souss Basin, Morocco, analysed by rainfall simulation and UAV remote sensing data, Catena, 113, 24–40, 2014.
Quinn, P. F., Beven, K. J., Chevallier, P., and Planchon, O.: The prediction of hillslope flow paths for distributed hydrological modelling using digital terrain models, Hydrol. Process., 5, 59–79, 1991.
Schürch, P., Densmore, A. L., Rosser, N. J., Lim, M., and McArdell, B. W.: Detection of surface change in complex topography using terrestrial laser scanning: application to the Illgraben debris-flow channel, Earth Surf. Proc. Land., 36, 1847–1859, 2011.
Servida, D., Grieco, G., and De Capitani, L.: Geochemical hazard evaluation of sulphide-rich iron mines: the Rio Marina district, J. Geochem. Explor., 100, 75–89, 2009.
Sperlich, M., Kattenborn, T., Koch, B., and Kattenborn, G.: Potential of unmanned aerial vehicle based photogrammetric point clouds for automatic single tree detection, Geoinformationen öffnen das Tor zur Welt, 26–28 March 2014, Hamburg, Germany, DGPF Tagungsband, 23, 2014.
Westaway, R. M., Lane, S. N., and Hicks, D. M.: The development of an automated correction procedure for digital photogrammetry for the study of wide, shallow, gravel bed rivers, Earth Surf. Proc. Land., 25, 209–226, 2000.

NHESSD
3, 6271–6319, 2015

Wheaton, J. M., Brasington, J., Darby, S. E., and Sear, D. A.: Accounting for uncertainty in DEMs from repeat topographic surveys: improved sediment budgets, Earth Surf. Proc. Land., 35, 136–156, 2010.

Ying Yang, M. and Förstner, W.: Plane Detection in Point Cloud Data, Department of Photogrammetry, Institute of Geodesy and Geoinformation University of Bonn, Bonn, Technical Report 1, available at: http://www.ipb.uni-bonn.de/technicalreports, last access: 7 October 2015, 2010.

Zevenbergen, L. W. and Thorne, C. R.: Quantitative analysis of land surface topography, Earth Surf. Proc. Land., 12, 47–56, 1987.

NHESSD

3, 6271–6319, 2015

Table 1. Information about all TLS epochs.

TLS Scanning campaign	Scan positions	Number of total points (unfiltered)	Number of total points (filtered)	Mean point density per 0.01 $m^2(\sigma)$ $m^{-2}(\sigma)$ (filtered data)	3-D-error of global reg. [m]	σ of the MSA reg. for scans of one time step [m]
Sep 2009	7	18 943 687	3 780 803	3.6(1.9)/288.1(165.5)		0.009–0.013
Apr 2012	11	46 542 218	5 386 857	4.7(2.0)/408.1(182.6)		0.007–0.011
Apr 2013	9	39 082 545	4 087 117	4.1(2.1)/330.2(185.5)	0.015	0.008–0.012
Apr 2014	8	31 984 062	4 192 532	4.2(2.0)/342.6(177.5)		0.008–0.011
Apr 2015	9	44 062 211	5 278 825	4.7(2.1)/396.3(195.3)		0.009–0.011

NHESSD
3, 6271–6319, 2015

Table 2. Information about both UAV epochs.

UAV campaign	Number of pictures	Number of tie points for exterior orientation	Number of total points (unfiltered)	Number of total points (filtered)	Mean point density per 0.01 $m^2(\sigma)$ $m^{-2}(\sigma)$ (filtered data)	Error of the exterior orientation [m]
Apr 2013	48	31	19 275 220	6 043 475	4.5(1.4)/418.2(114.6)	0.034
Apr 2015	158	37	60 016 606	5 925 190	4.5(1.4)/418.2(114.6)	0.048

NHESSD
3, 6271–6319, 2015

Table 3. Standard deviation and LoD (at a 95 % confidence interval) in meter for the single TLS and UAV epochs derived on the base of the stable areas.

Method	TLS								UAV (TLS)	
Epoch	2009–2012		2012–2013		2013–2014		2014–2015		2013–2015	
	σ	LoD	σ	LoD	σ	LoD	σ	LoD	σ	LoD
	0.035	0.097	0.013	0.036	0.036	0.100	0.015	0.042	0.039 (0.035)	0.108 (0.097)

NHESSD
3, 6271–6319, 2015

Table 4. Sediment balancing (only values over the LoD) for the area of interest (AoI) and separated for the slopes and the reservoir for all epochs of the TLS measurements.

Epoch	AoI cut	AoI fill	AoI balance	slope balance	reservoir balance
2009–2012	−75.41 m^3	30.78 m^3	−44.62 m^3	−65.82 m^3	20.58 m^3
2012–2013	−32.37 m^3	59.76 m^3	27.39 m^3	32.37 m^3	−2.65 m^3
2013–2014	−47.28 m^3	90.80 m^3	43.52 m^3	−23.3 m^3	64.58 m^3
2014–2015	−55.71 m^3	127.90 m^3	72.19 m^3	35.50 m^3	36.39 m^3
2009–2015	−188.28 m^3	191.54 m^3	3.26 m^3	−134.61 m^3	137.96 m^3
2013–2015	−82.15 m^3	176.33 m^3	94.18 m^3	−21.70 m^3	118.45 m^3

NHESSD
3, 6271–6319, 2015

Table 5. Volume balancing based on the UAV data for the whole AoI.

Epoch	cut	fill	balance
2013–2015	$-123.86\,m^3$	$80.65\,m^3$	$-43.21\,m^3$

NHESSD
3, 6271–6319, 2015

Table 6. Volume balance based of the UAV and the TLS data for the whole AoI.

Method	Epoch	cut	fill	balance
UAV	2013–2015	−123.86 m^3	80.65 m^3	−43.21 m^3
TLS	2013–2015	−82.15 m^3	176.33 m^3	94.18 m^3

NHESSD
3, 6271–6319, 2015

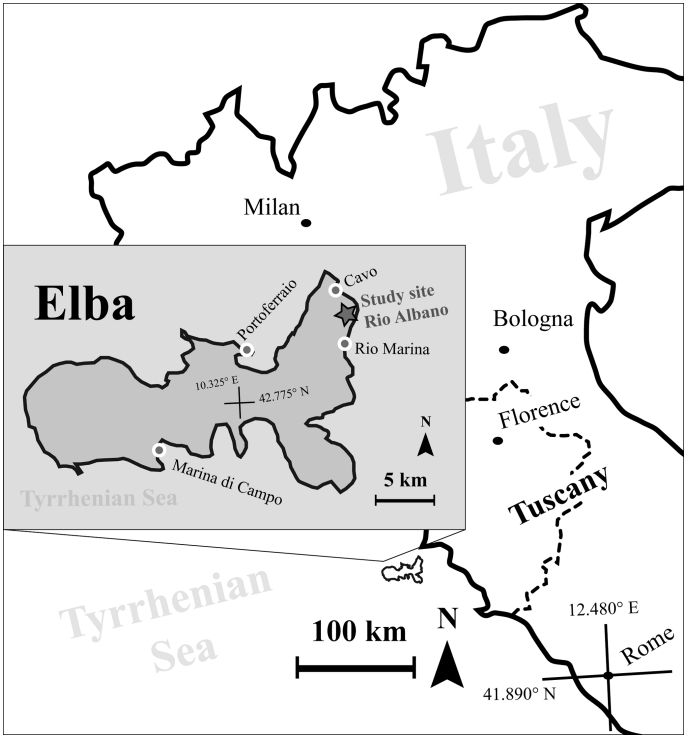

Figure 1. Location of the study area.

NHESSD
3, 6271–6319, 2015

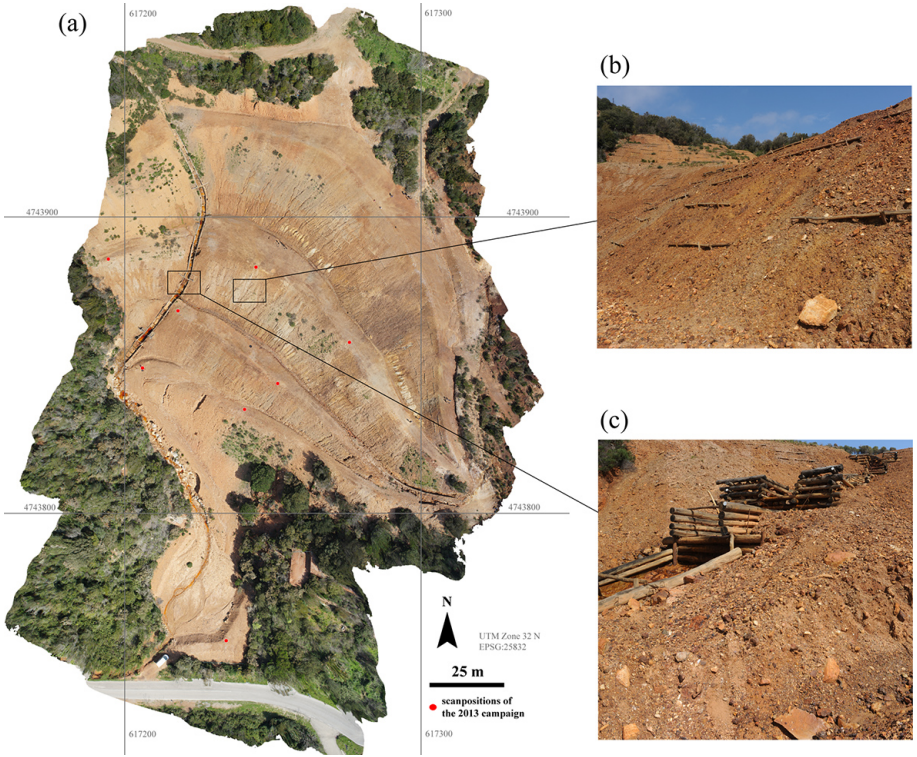

Figure 2. (a) Orthorectified and referenced aerial photograph (by the 2013 UAV campaign, ground resolution 5 cm) of the investigated slope with the 2013 scanning positions, **(b)** the artificial barriers on the slope and **(c)** a part of the main artificial drainage channel.

NHESSD
3, 6271–6319, 2015

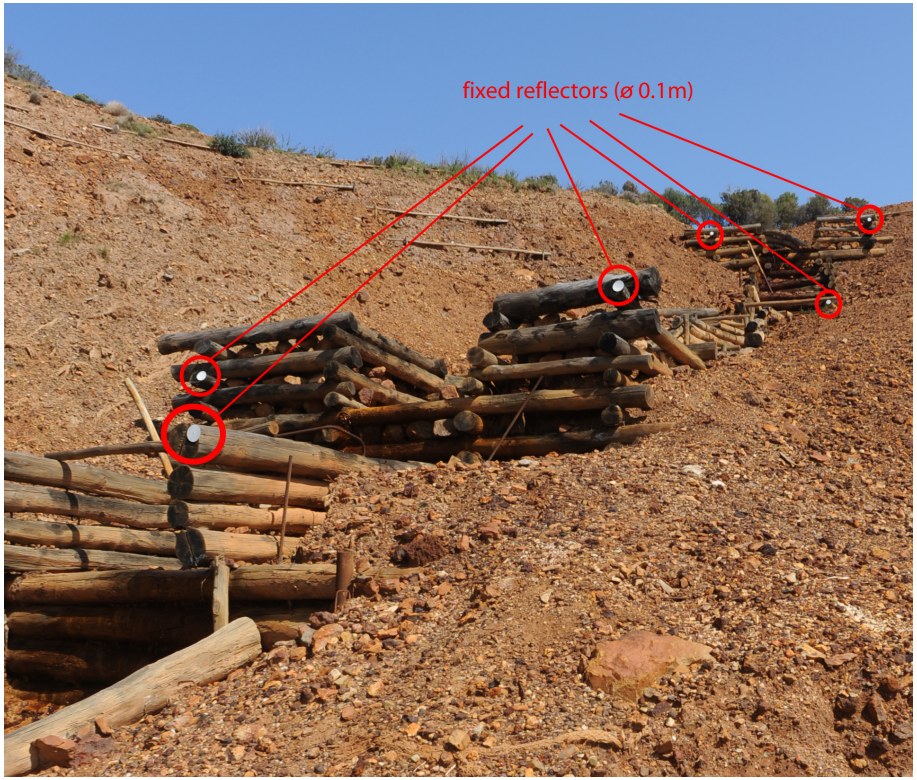

Figure 3. Picture of the mounted tie points on the debris flow barrier.

NHESSD
3, 6271–6319, 2015

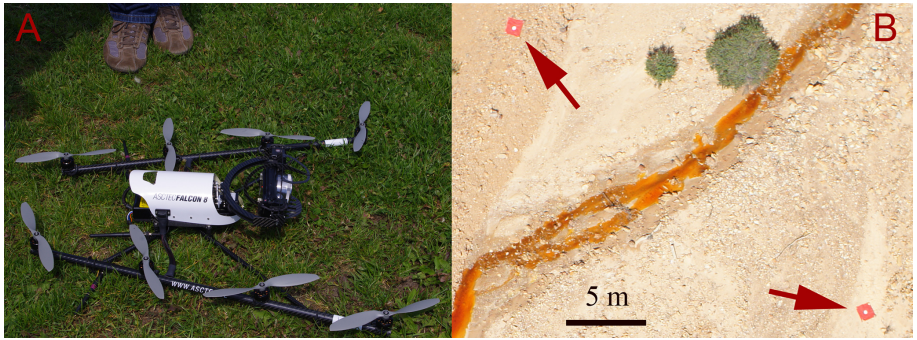

Figure 4. (a) The Astec Falcon 8 UAV and **(b)** carpets with reflectors used as GCP's for exterior orientation.

NHESSD
3, 6271–6319, 2015

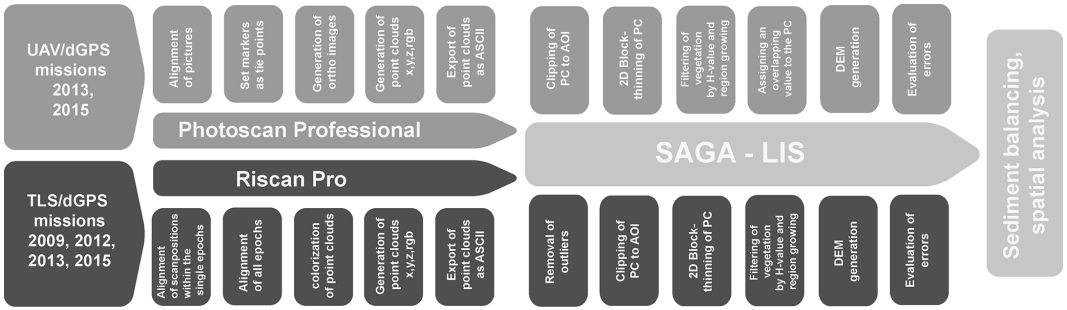

Figure 5. Workflow of the processing steps in Photoscan Professional, Riscan Pro and LIS/SAGA GIS.

NHESSD
3, 6271–6319, 2015

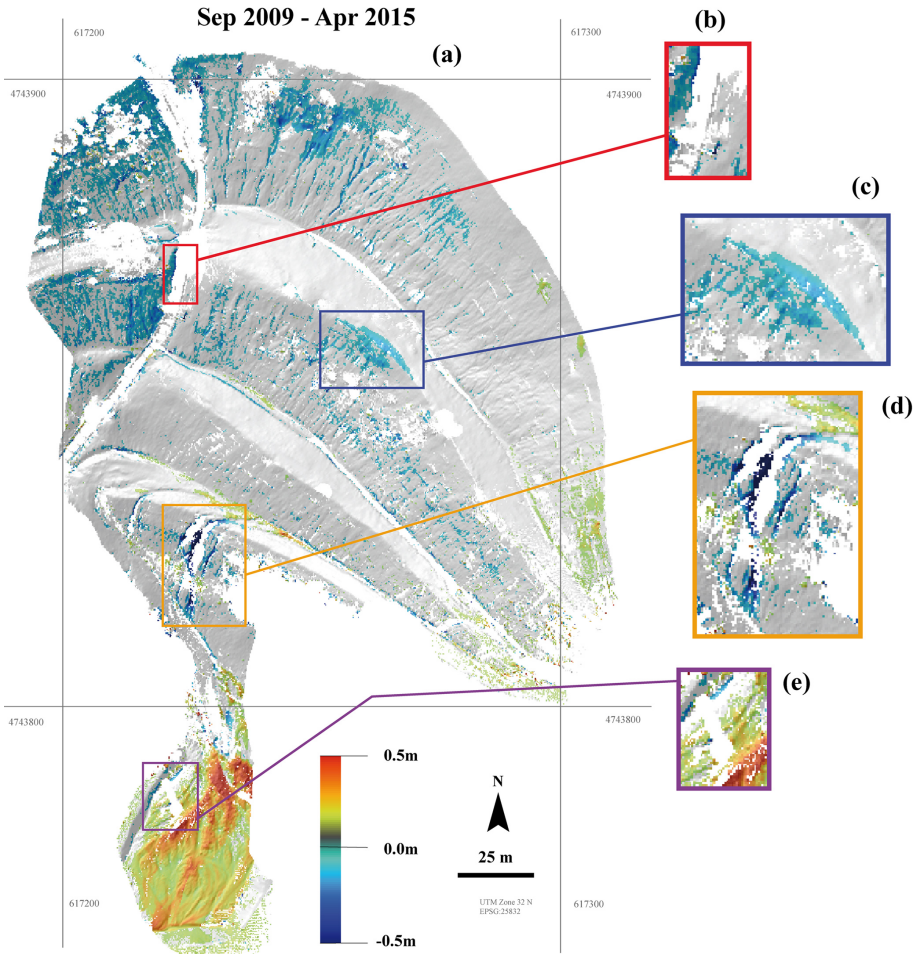

Figure 6. Surface changes (over the LoD) on the AoI for the 2009–2015 epoch of the TLS measurements.

NHESSD
3, 6271–6319, 2015

Investiagtion of geomorphic processes on the Italian island Elba by LiDAR and UAV

F. Haas et al.

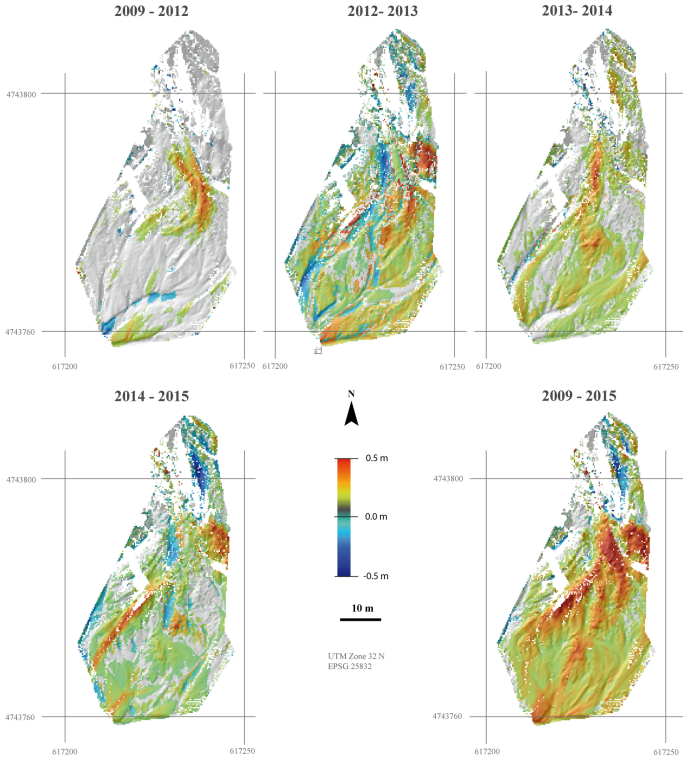

Figure 7. Surface changes (over the LoD) in the reservoir for the single epochs between 2009 and 2015.

NHESSD
3, 6271–6319, 2015

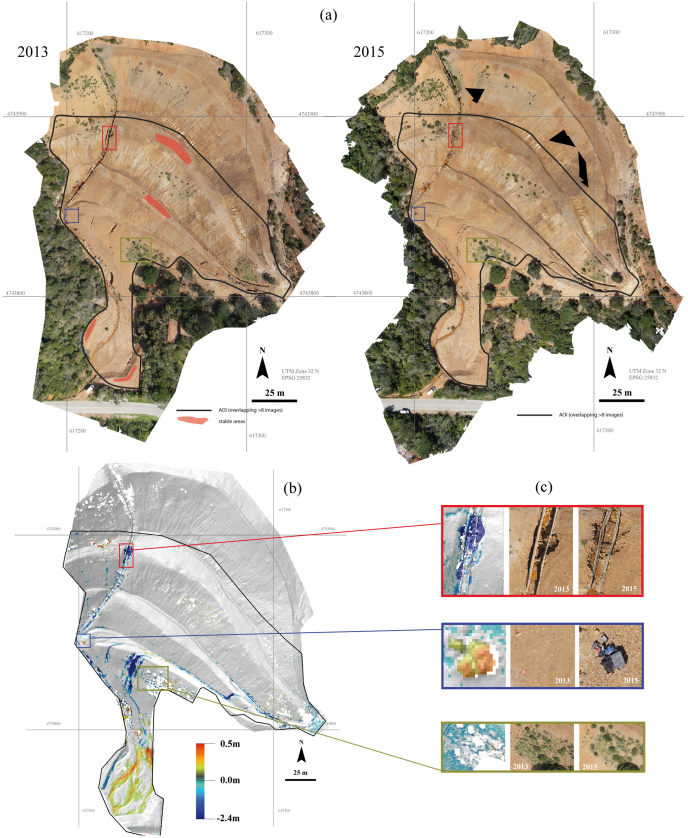

Figure 8. (a) Aerial Photographs of the 2013 and 2015 UAV epochs with the AOI and the stable areas used for error estimation, **(b)** the surface changes for the period 2013–2015 for the AOI and **(c)** enlargements of special areas/features.

NHESSD
3, 6271–6319, 2015

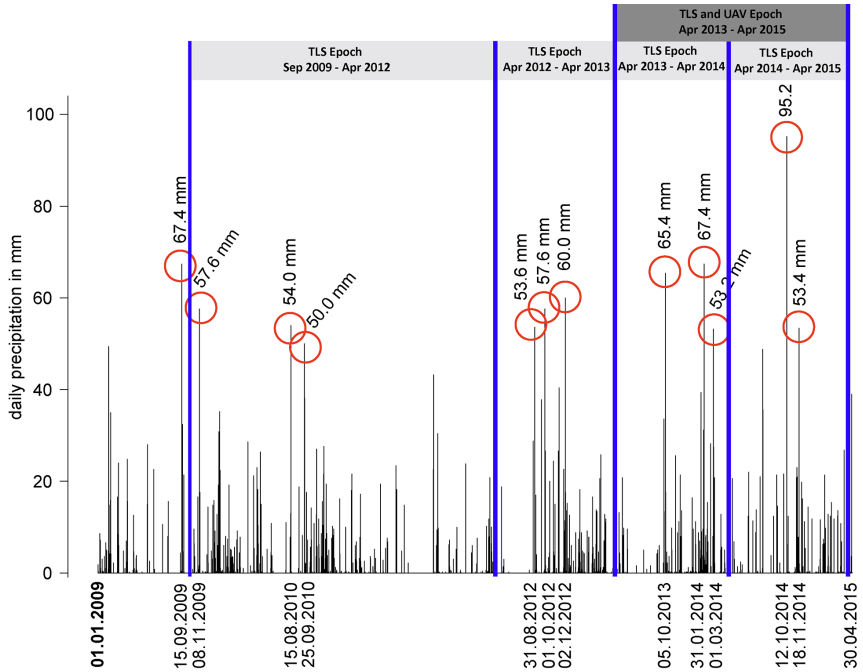

Figure 9. Daily precipitation at the Meteo Station *Vecchia Aurelia* in the Northeast of Piombino (UTM coordinates: 631 512.00 E 4 764 190.00 N) for the period April 2009 – April 2015, provided by the *Servizio Idrologico Regionale* (sir.toscana.it).

NHESSD
3, 6271–6319, 2015

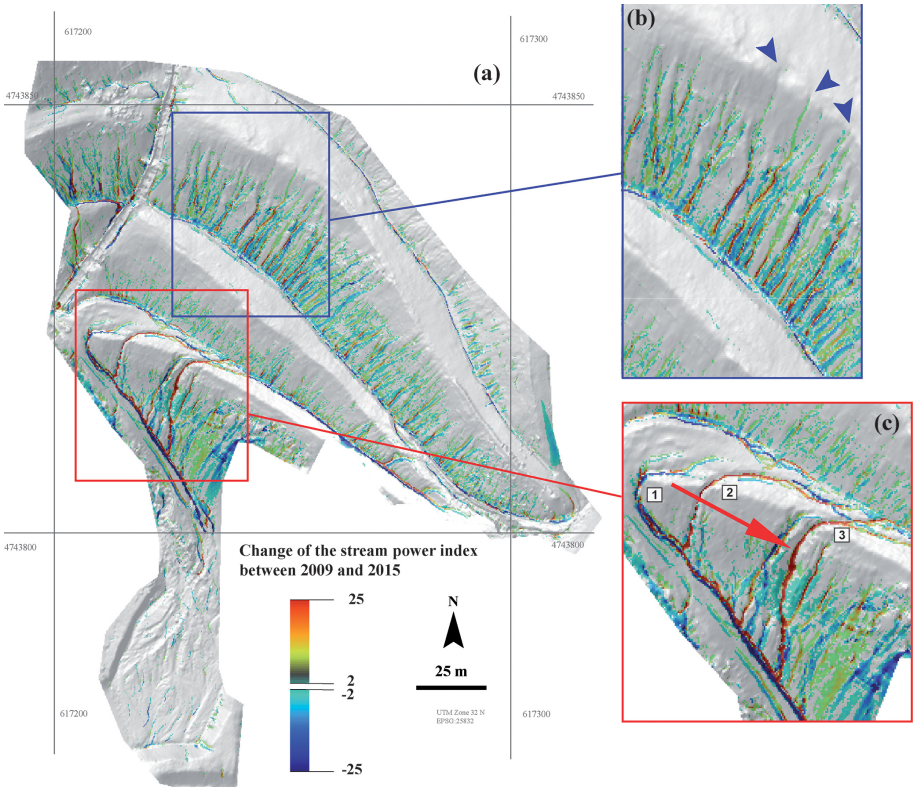

Figure 10. (a) Change of the stream power index between 2009 and 2013 for the slope (for better visualisation data from −2 to 2 are excluded), **(b)** back-cutting of channels up to the top of the terrace indicated by the SPI and **(c)** shifting of the main channel/gully from west to the east with increasing SPI.

NHESSD
3, 6271–6319, 2015

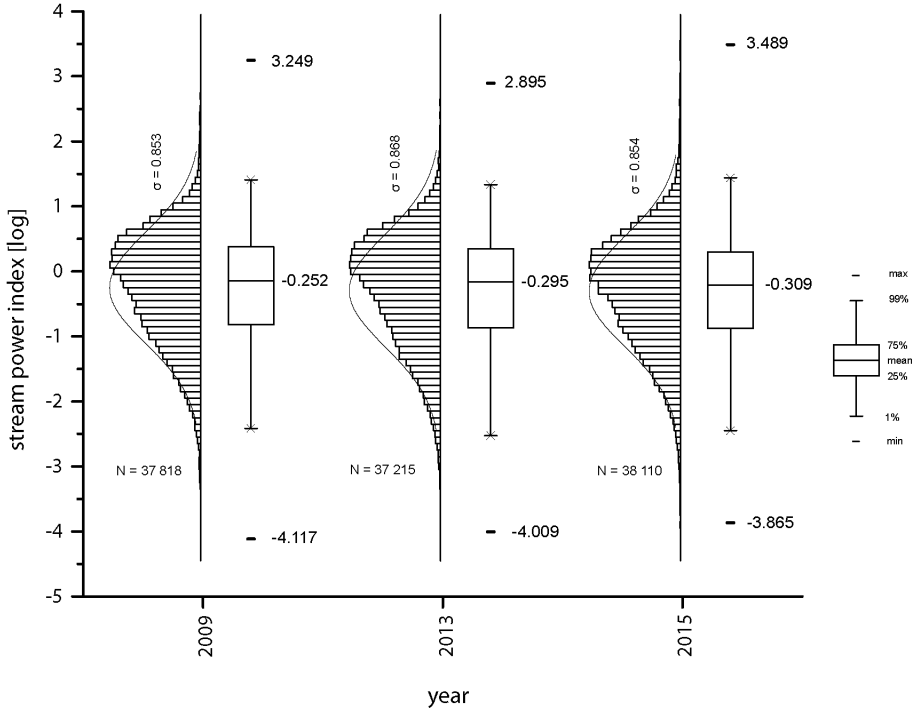

Figure 11. Box-plot and statistical distribution of the SPI for the epochs 2009 (TLS), 2013 and 2015 (both UAV).

NHESSD
3, 6271–6319, 2015

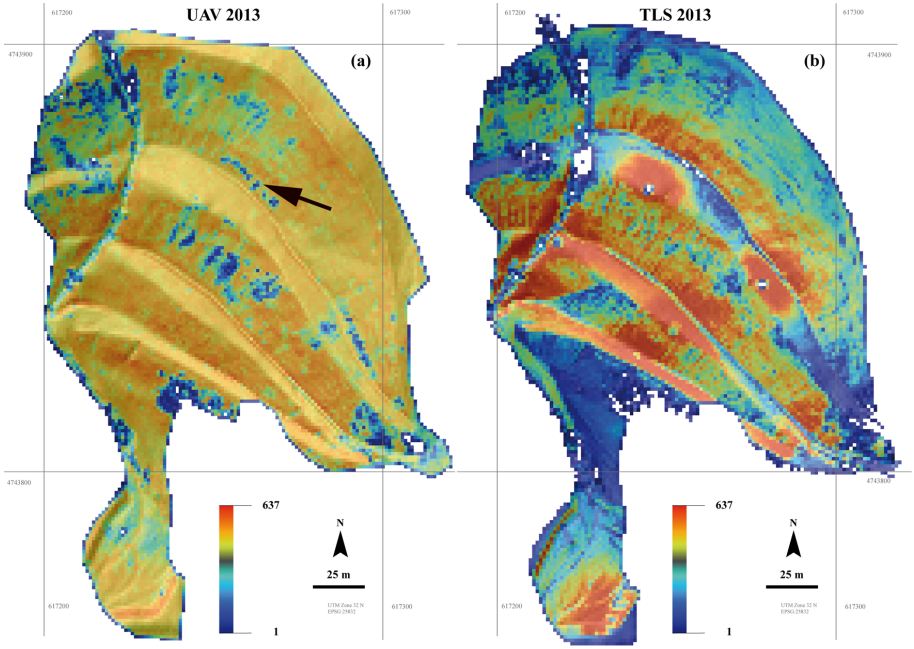

Figure 12. Comparison of the point density (points m^{-2}) for **(a)** the 2013 UAV data and **(b)** the 2013 TLS data.

NHESSD
3, 6271–6319, 2015

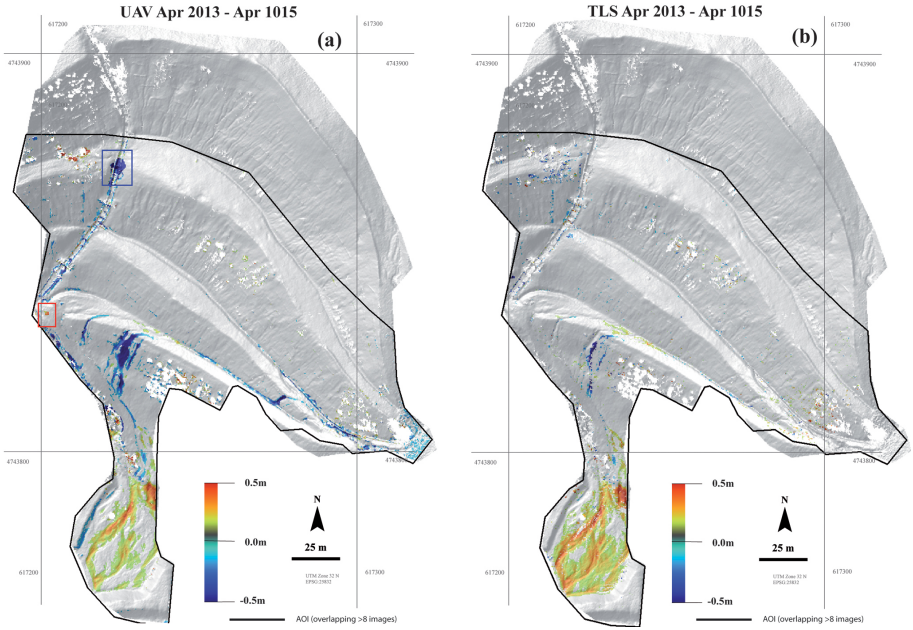

Figure 13. Comparison of the surface changes of the 2013 to 2015 epoch for **(a)** the UAV data and **(b)** the TLS data.

NHESSD
3, 6271–6319, 2015

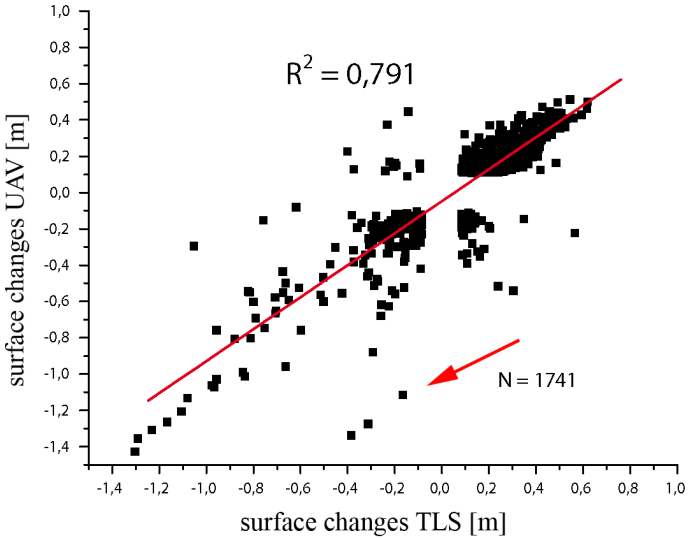

Figure 14. Comparison of surface changes of the 2013 to 2015 epoch for the UAV and the TLS data, which are detected in both datasets.

NHESSD
3, 6271–6319, 2015